Droplet impacting a superhydrophobic mesh array: Effect of liquid properties

Geng Wang, Jingqi Gao, and Kai H. Luo*
Department of Mechanical Engineering, University College London, Torrington Place, London WC1E 7JE, England, UK

(Received 17 August 2020; accepted 30 November 2020; published 23 December 2020)

Generation of monodisperse droplets by a large droplet impacting a mesh array is a common technique in microfluidic engineering, materials science, and drug production. Understanding the dynamic mechanism behind this is critical to controlling this process. This work uses a nonorthogonal multiple-relaxation-time lattice Boltzmann (LB) method to simulate a droplet impacting a mesh array. By varying the droplet viscosity and surface tension, a comprehensive parametric study is carried out to investigate the influence of droplet properties on the dynamic process of droplet impact, penetration, and fragmentation. The results indicate that the inertial effect dominates the spread stage of droplet impact. At later stages, the viscous drag and surface tension act to prevent the spread of the droplet, which results in different maximum spreading diameters. The penetration of the droplet through the mesh initially leads to the formation of a liquid jet, the length of which is determined by the competition between the dynamic pressure and capillary pressure. Different jet breakup lengths are observed for various Weber numbers. The maximum spreading diameter and jet breakup length are predicted by an extended model over a wide range of liquid properties, in good agreement with the LB simulation results. An analysis is also conducted from an energy perspective. It is found that the surface energy significantly decreases after the fragmentation of the high-viscosity droplet, which is caused by the merge of satellite droplets after the jet breakup.

DOI: 10.1103/PhysRevFluids.5.123605

I. INTRODUCTION

The impact of a liquid droplet on a superhydrophobic surface has been intensively studied, owing to its self-cleaning, antifouling, and drag-reducing potentials [1–6]. In particular, the formation of monodisperse droplets, by a drop or drops impacting a mesh array with pores of tens to hundreds of microns in dimension, is one of the most promising techniques [7,8]. This configuration has a wide range of applications in microfluidic engineering [9,10], materials science [7,8], and agriculture [11]. Examples include three-dimensional (3D) inkjet printing of dental prostheses [12], living cell microarrays [13], and ceramic suspensions [14]. Recently, Modak *et al.* [15] reported a drop-on-demand printing technique based on this configuration, which offers several advantages over inkjet printing. Parameters such as the maximum droplet spreading diameter, liquid jet breakup length, and droplet-penetrated mass are crucial for the novel material development and microfluid control [7–11,16]. According to previous theories, the droplet would go through complex dynamic processes, including collision, penetration, and fragmentation, when interacting with the hydrophobic orifice plate [11,16,17]. Despite various studies for more than a century, many

*Corresponding author: k.luo@ucl.ac.uk

phenomena associated with this complex process remain poorly understood, such as the jet breakup dynamics and irregular distributions of satellite drop sizes [8,9].

The rapid development of experimental high-speed imaging technologies has led to the unravelling of some of the knowledge gaps in this area [9–11,16]. Brunet *et al.* first captured the secondary droplet generation in their experiments of a droplet impacting on a hydrophobic microgrid and investigated the effects of the grid geometry [10]. Ryu *et al.* [18] and Xu *et al.* [19] investigated the droplet penetration mechanism during the impact of a water droplet through a mesh screen. Ryu *et al.* [18] indicated that a superhydrophobic mesh enhanced droplet penetration through the mesh compared to a hydrophobic mesh. Xu *et al.* [19] asserted that the droplet collision process was determined by the competition between the inertial pressure and water hammer pressure. In the field of materials science, and Kumar *et al.* [7] and Zhang *et al.* [8] carried out experimental research into water droplets impacting superhydrophobic textiles. The influence of the droplet impact speed on the maximum droplet spreading diameter, contact time, and the penetrated mass was analyzed. In the studies of Kooij *et al.* [9] and Soto *et al.* [11], they applied simplified assumptions to propose a model for the prediction of the water-droplet-penetrated mass and the maximum spreading diameter after impacting the mesh screen.

Most of the existing researchers have adopted experiment methodologies [9,20] which provide qualitative rather than quantitative results due to experimental limitations [7–11]. Important physical insights into complex two-phase flow regarding the velocity distribution within the liquid and the energy evolution in the dynamic process are currently inaccessible by experimental techniques. Also, deviations are common in controlling the droplet landing position and impact velocity in the experiment [21]. In recent years, numerical simulation techniques have started to be applied to studies of droplet impact on mesh screens due to accurate control of physical parameters and access to quantitative information. In 2019, Wang *et al.* [21] used a many-body dissipative particle dynamics (MDPD) method to simulate water droplet fragmentation after impacting on mesh screens and determined the droplet ejection angle and the penetrated mass. More recently, Vontas *et al.* [20] adopted the volume-of-fluid (VOF) method to investigate droplet impact on various mesh screens.

In the existing studies of this configuration, the impact dynamics of water droplets were widely investigated [7–11]. However, the influence of droplet properties has not been systematically researched [9]. One exception was the study of Vontas *et al.* [20], which tested a water, acetone, and glycerol mixed droplet impacting a mesh. However, the dimensionless Ohnesorge number in their study was less than the critical value 0.018 [20,22] below which the viscosity effect is negligible in the droplet dynamics. Therefore a knowledge gap still exists in this configuration, especially for the high-viscosity droplet. In the present study we adopt a nonorthogonal multiple-relaxation-time (MRT) lattice Boltzmann (LB) method [23] to systematically investigate the effects of droplet properties on the dynamics of droplets impacting a superhydrophobic mesh array. By analyzing the force balance and energy evolution, the mechanisms behind droplet spread, penetration, and fragmentation are investigated. Furthermore, the maximum spreading diameter and the liquid jet breakup length after the impact will also be predicted. In the following section, the simulation methodology, computational setups, as well as numerical model validations are presented. Section III presents the simulation results, providing a detailed analysis of droplet dynamics and energy evolution. The conclusion of this study will be presented in Sec. IV.

II. METHODOLOGY

A. The lattice Boltzmann multiphase model

As a kinetic-theory-based mesoscopic numerical method, the LB method has been widely adopted in the simulation of complex fluids [24–26]. It has the advantages of simple and robust numerical algorithm, high parallel efficiency, ease of incorporating mesoscopic and microscopic physics, and ability to handle complex configurations [27–29]. Especially in the simulation of the multiphase flow, the interface deformation, breakup, and merge can be captured naturally [27,28].

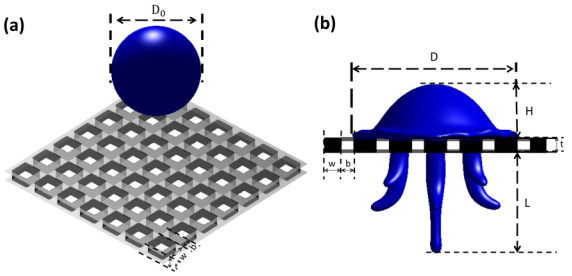

FIG. 1. The 3D main view (a) and side view (b) of a liquid drop impacting a mesh array.

And the interaction between the liquid phase and various types of surfaces can be described with simple boundary treatment [30–32]. Compared with the conventional multiphase simulation methods such as the VOF, the LB method is computationally an order of magnitude more efficient and produces one to three orders of magnitude lower spurious currents at interfaces [33]. On the other hand, the basic implementation of the LB method for multiphase flow suffers from numerical instabilities when high density ratio, large Weber number, and/or Reynolds number are involved [23,24,28].

In this study we adopt a recently proposed nonorthogonal MRT-LB model [23] to enhance numerical efficiency and stability. To treat the multiphase flow, an improved pseudopotential model proposed by Li *et al.* [31] is employed. The superhydrophobic wettability conditions are realized by the model proposed by Li *et al.* [32]. The nonorthogonal MRT-LB multiphase framework has been validated in several studies such as [17,23] for its numerical efficiency and stability as well as simulation fidelity in comparison with experimental results. In the following, the method will be further validated against experimental data in Ref. [7]. The details of the model can be found in the Appendix.

B. Simulation setup

Figure 1(a) is the three-dimensional physical configuration of the droplet and mesh array assembly, where D_0 denotes the initial droplet diameter, w represents the opening width, b indicates the solid width, and the thickness of the array t equals w. Figure 1(b) is the side view during the droplet penetration; the diameter of the pancake which remains above the mesh is D. The height of the pancake is H, and L indicates the length of the liquid jet which penetrates below the mesh.

Considering the liquid properties are the research interest in this work, for the convenience of the comprehensive parametric study, the dimensionless quantities are employed. The Weber number ($\mathrm{We} = D_0 V^2/\gamma$), which represents the ratio of inertial force and capillary force, is used to evaluate the influence of the droplet surface tension. The Ohnesorge number ($\mathrm{Oh} = \mu/\sqrt{D_0 \gamma \rho_l}$) is adopted to evaluate the influence of the viscous force relative to the mean of inertial and capillary forces. ρ_l, γ, μ, V are the density, surface tension, dynamic viscosity, and impact velocity of the droplet, respectively. The solid fraction (ϕ) of the mesh array is set as $\phi = 1 - [w/(w+b)]^2$. The effect of gravity is negligible in this study because droplet diameter is below the inertial capillary length $L_c =$ 2.7 mm [34,35]. The dimensionless time is defined as $T^* = V \times N/D_0$, where N is the number of simulation time steps, and $T^* = 0$ represents the moment when the droplet starts to touch the mesh array. The dimensionless values of pancake's diameter (D^*), pancake's height (H^*), as well as liquid jet length (L^*) are adopted in the following analysis, which are all defined with respect to the initial droplet diameter.

The grid independence study is conducted by simulating a droplet impacting a mesh array under various grid resolutions. The resolutions of droplet radius (R) are set as 45, 60, and 70 lattice units, respectively. All the other parameters are kept the same. The grid number in X and Z directions is 8 and 20 times the droplet radius, respectively, and the grid number in the Y direction equals that in

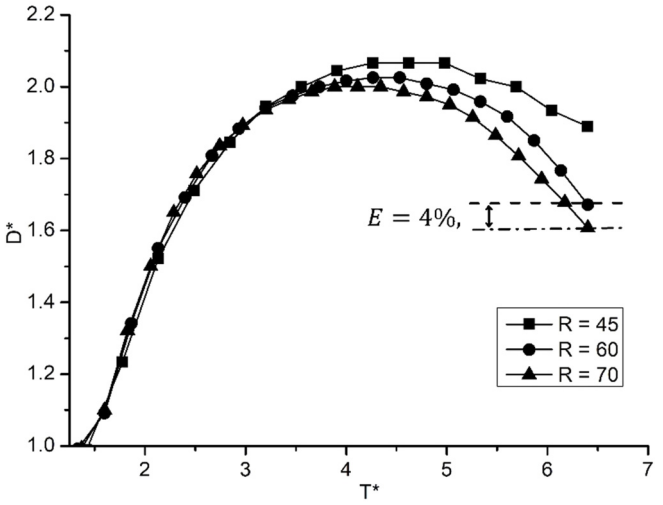

FIG. 2. The dimensionless pancake diameter evolution after impacting the mesh array for various droplet radius resolutions.

the X direction. The ratio between the opening width and the droplet radius is fixed at 0.43, and the solid fraction (ϕ) of the mesh is kept at 0.6. The Weber and Ohnesorge numbers are kept at 150 and 0.04, respectively. Figure 2 indicates the evolution after the droplet touches the mesh.

As shown in Fig. 2, significant deviations are observed for the $R = 45$ case because of insufficient grid points in the opening. For the $R = 60$ and 70 cases, the maximum relative error for the results $E = |D^*(60) - D^*(70)|/D^*(70) \times 100\%$ is less than 4%, and the grid resolution has little influence on the simulation results. Thus, in the following simulations, over 60 grid points are used for the droplet radius and over 25 grid points for the mesh opening.

C. Model validation

Validation of the LB model is conducted with reference to experimental results of [7], which simulated a 2.5-mm-diameter water droplet impacting a superhydrophobic sieve. The wire breadth and opening width of the mesh sieve equal 0.3048 and 0.5334 mm, respectively, while the contact angle (CA) equals 162°. The ratio of the opening width to the droplet radius and the solid fraction (ϕ) of the mesh are 0.43 and 0.6. Using the lattice units, the droplet diameter (D_0), the opening width (w), and the solid width (b) are set up as 120, 26, and 15, respectively. To capture all the features of the droplet impact on the mesh, we set up the simulation domain in x, y, and z directions to be 4, 4, and 10 times the droplet diameter, respectively, and the total grid points are over 250 million. Considering that the viscosity effect of the water droplet can be ignored under the experimental conditions, the liquid kinematic viscosity for the validation cases is then set to be smaller than 0.0075 in the lattice units so that the Ohnesorge number (Oh) < 0.008. Firstly, the simulation and experiment results are qualitatively compared for two Weber numbers. Figure 3(a) shows the We = 54.4 case and Fig. 3(b) the We = 204 case.

As shown in the qualitative comparison, the simulation and experimental results are in good agreement. After droplet impact on the plate, the pancake above the mesh array spreads horizontally along the mesh and then retracts. In the meantime, part of the liquid penetrates throughout the mesh to form liquid jets or fingers. For the higher We case, the maximum spreading diameter of the pancake is larger, and the breakup length of the liquid jet is longer. Owing to difficulties in the precise control of the initial impact speed and center location of the droplet in the experiment

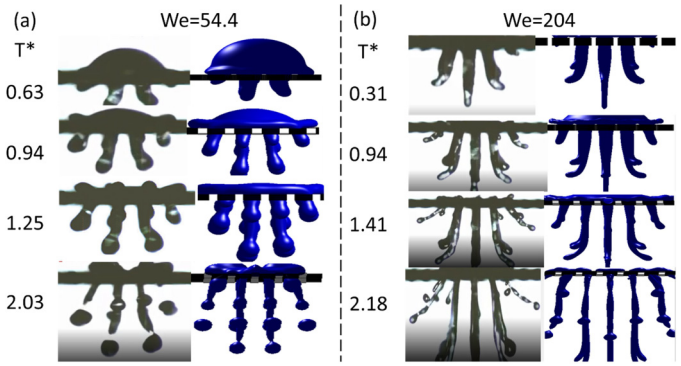

FIG. 3. Comparison between the experimental snapshots (gray) [7] and the present LB simulation (blue) of water droplets impacting a superhydrophobic mesh array for two Weber numbers.

[7], small deviations between the simulation and experimental snapshots can be found in the jet fragmentation as well as the pancake splashing shape.

Considering constant geometric parameters of the mesh array in the present study, and the computational cost constraint, further quantitative comparisons are conducted in the same configuration with different Weber numbers. The maximum spreading diameter of the pancake [Fig. 4(a)], breakup time, contact time, and spread time [Fig. 4(b)] have been recorded and compared with the results from Ref. [7]. The maximum spreading diameter and the time are nondimensionalized by the initial droplet diameter and inertia-capillarity time ($\tau = {D_0}^3 \rho_l / \gamma)^{0.5}$, respectively.

As shown in Figs. 4(a) and 4(b), in terms of the quantitative comparison, the simulation results are also in good agreement with the experimental data for a wide range of We. Thus the present model is proved to be capable of accurately simulating a droplet impacting the mesh array. Besides the current results, more qualitative and quantitative validations of the proposed simulation methodology were performed in Refs. [17,23].

III. SIMULATION RESULTS AND DISCUSSION

To further investigate the influence of liquid properties in the droplet impact on the mesh array, simulations are conducted under different Weber and Ohnesorge numbers. In the following

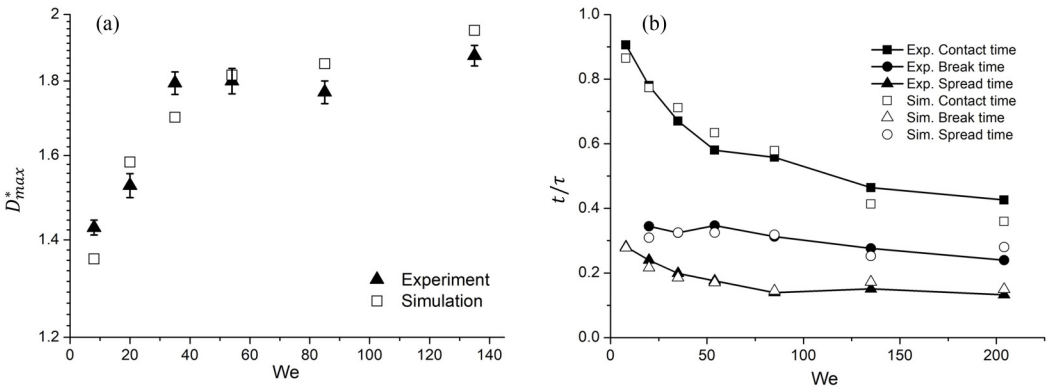

FIG. 4. Comparison of the maximum dimensionless spreading diameter for experimental and simulation results (a) and comparison of the dimensionless contact time, break time, and spread time for experimental and simulation results (b).

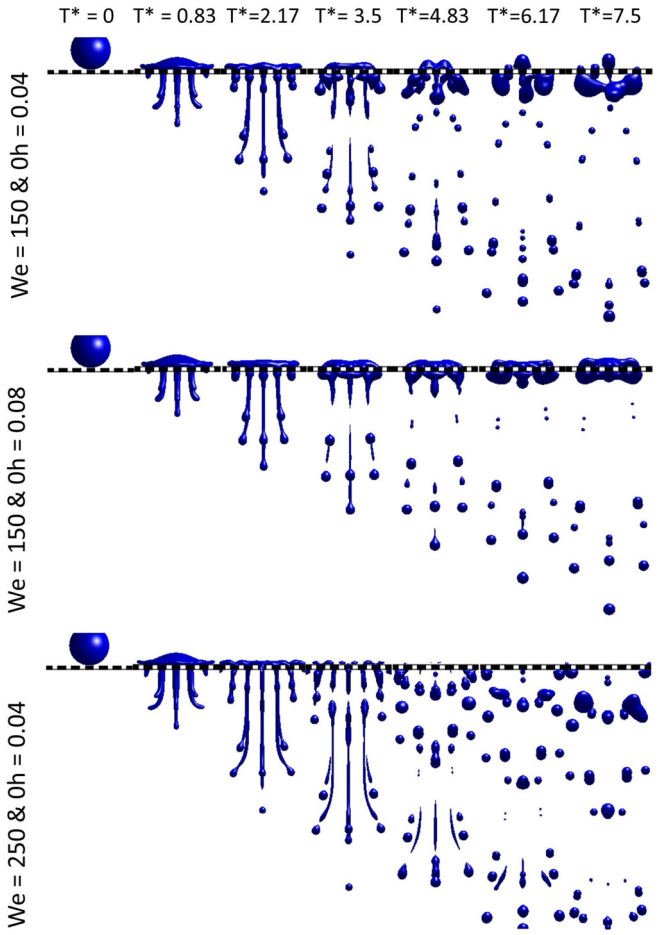

FIG. 5. Dynamics of droplet impacting a mesh array under various conditions: (a) We = 150 and Oh = 0.04, (b) We = 150 and Oh = 0.08, and (c) We = 250 and Oh = 0.04.

simulations, the geometric parameters of the mesh array, as well as the ratio between the opening width and the droplet radius, are kept the same as in Secs. II B and II C. And the droplet impact velocity (V) and initial droplet diameter (D_0) are all fixed as 0.08, 120 in the lattice units. The density ratio and the kinematic viscosity ratio between the liquid phase and the gas phase are kept at 500 and 10, respectively. Under low We, the droplet shows the nonpenetration state [8], which is outside of our research interest. And with high We, the elasticity of the mesh wire cannot be ignored [21], thus the medium We cases were investigated. By changing the droplet surface tension and viscosity, We is varied from 75 to 300 and Oh is between 0.02 and 0.08. The static contact angle between solid and liquid θ is fixed at 155° to reach the superhydrophobic condition.

Figure 5 demonstrates the droplet evolution process for the various We and Oh cases. After impacting on the mesh, the droplet takes the shape of a pancake in all cases. Then the pancakes spread horizontally above the mesh array at a different rate depending on the values of Weber and Ohnesorge numbers. Below the pancake, liquid penetrates through the mesh and forms liquid jets below the mesh plate continuously. The liquid jets then break up and form satellite droplets. Figures 5(a) and 5(c) indicate the maximum pancake spreading diameter increases with We, in agreement with the results in Refs. [7,8]. In contrast, the maximum pancake spreading diameter decreases with Oh, as shown in Figs. 5(a) and 5(b), which is similar to the finding from a droplet

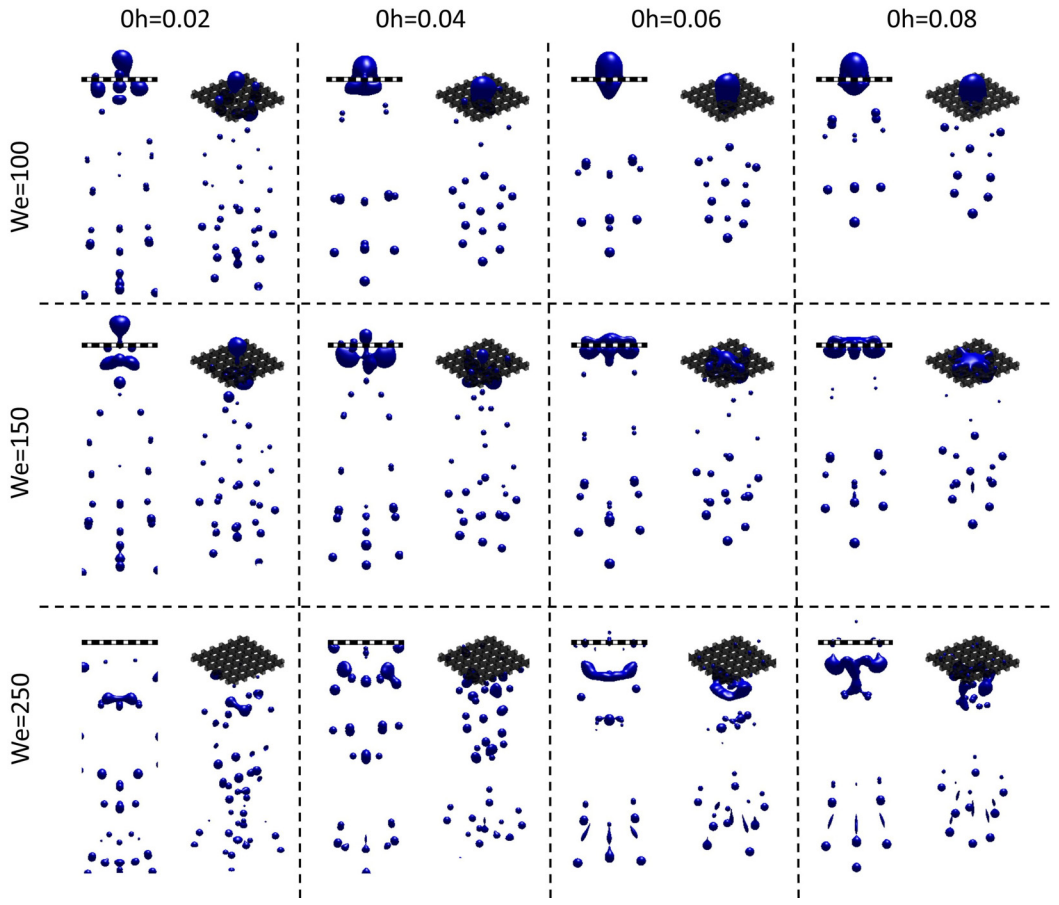

FIG. 6. The 3D main view and side view of droplet fragmentation after impact on the mesh array. The rows in the figure represent different We cases, and the columns indicate various Oh cases.

impacting a solid flat plate [36]. By comparing the evolution of the liquid jets below the mesh plate, it can be observed that the maximum breakup lengths of the liquid jets significantly increase with We, in agreement with the findings in Refs. [37,38]. It is also noted that the maximum breakup lengths decrease slightly with increasing Oh. As the pancake spreads over the mesh, the liquid penetrates through the mesh openings simultaneously. Moreover, the higher the Weber number, the higher the pancake spread rate and the higher the penetration rate. On the contrary, the higher the Ohnesorge number, the lower the pancake spread rate and the lower the penetration rate.

Figure 6 includes the main view and side view of droplet fragmentation under various Weber and Ohnesorge numbers when $T^* = 6.5$. Similar to the experimental results, the droplet total penetrated mass increases with We [11,21] but decreases with Oh [20], which is also in agreement with the pancake's penetration rate indicated in Fig. 5. In terms of satellite droplets after the liquid jet breakup, the number significantly increases with We but decreases with Oh, and the size of the satellite droplets has an uneven distribution. The simulation results confirm the conclusion in Ref. [9] that the spray from the droplet impacting the mesh is governed by the jet instability, and the breakup of the capillary jets causes a broad droplet size distribution [9,39].

As indicated in the above qualitative results, the liquid properties affect the droplet spread and penetration dynamics, and lead to various fragmentation outcomes. In the following, quantitative analysis will be conducted to investigate the influence of droplet properties. Firstly, the height and

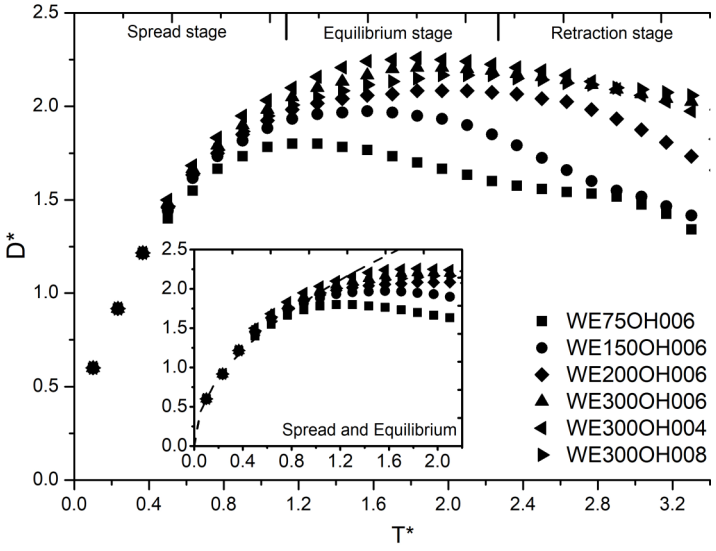

FIG. 7. The dimensionless pancake diameter as a function of dimensionless time. The evolution is divided into three stages: spread stage, equilibrium stage, and retraction stage. The evolution of the spread stage in the inserted figure agrees with the theoretical prediction of Eq. (1) (dashed line).

diameter of the pancake, and the jet length, will be investigated below. Secondly, based on the energy analysis, the droplet surface area evolution and fragmentation mechanisms will be presented.

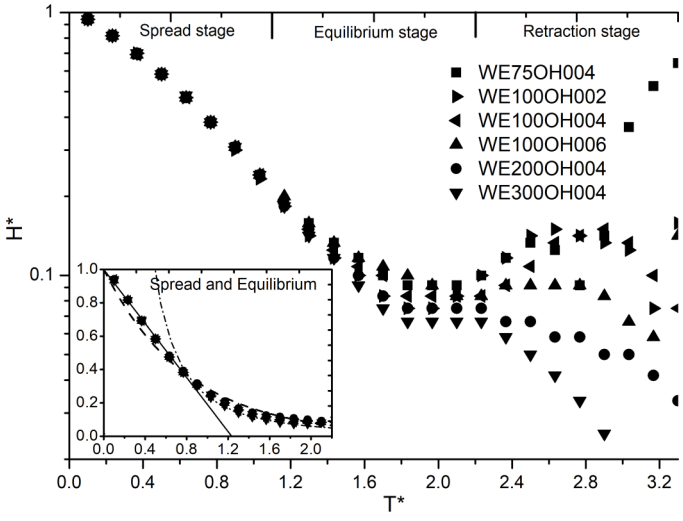

FIG. 8. The dimensionless pancake height vs the dimensionless time during the three stages. The insert figure shows the spread stage and equilibrium stages of the pancake's height evolution: the dash-dotted line stands for the power law dependency, the solid line represents linear dependency, and the dashed line demonstrates the exponential decay dependency [Eq. (2)].

A. Droplet dynamic evolution

The pancake's diameter and height evolution are shown in Figs. 7 and 8, respectively. In the figures, the x axis stands for the dimensionless time (T^*) and the y axis denotes the dimensionless diameter (D^*) and height (H^*) of the pancake, respectively. The evolution process is divided into three stages, which are spread stage, equilibrium stage, and retraction stage.

As indicated in Fig. 7, the pancake diameter rapidly increases to the peak value in the spread stage to reach a quasiequilibrium. The maximum pancake spreading diameter varies with Oh and We, and the retraction time varies in different cases and is significantly lower for the smaller We droplets. This is because the bounce off time of the droplet is proportional to the dimensionless inertia-capillarity time ($\tau^* = \mathrm{We}^{0.5}/2$) [40]. During the spread stage, the droplet dynamics for all cases are very consistent, as these are governed by the inertial effect which is determined by the impact velocity. The temporal change of the pancake diameter has been discussed in previous studies [8,41]:

$$D^* = C_1 T^{*0.5}. \tag{1}$$

The fitted constant C_1 in our study equals 1.92, which is similar to the experimentally fitted constant 2.8 in Ref. [41]. As shown in the insert of Fig. 7, the simulation results in all cases achieve a good agreement with the theoretical prediction [the dashed line represents Eq. (1)].

Regarding the evolution of pancake's height, as indicated in Fig. 8, it first decreases in the spread stage and then reaches a quasiequilibrium, followed by a retraction stage. For the lower We cases, the rebound droplet leads to an increase in the pancake's height in the retraction stage. In the higher We cases, the droplets penetrate through the mesh array, resulting in the continuous decrease in the pancake's height.

Three different models are adopted to describe the height evolution of the pancakes during the spread and the equilibrium stages. These are shown in the insert of Fig. 8: the power law dependency $H^* = AT^{*-2}$ [42,43], linear dependency $H^* = 1 - BT^*$ [8], and exponential decay dependency [9]:

$$H^* = e^{-C_2 T^*}. \tag{2}$$

As indicated in Fig. 8, the simulated droplet height evolution agrees well with the power law at the later spread stage and the equilibrium stage, and the best fitted constant A equals 0.24, which is of the same magnitude as that in Ref. [42]. Similar to the results in Refs. [8,42], the simulated evolution of the droplet height at the early stage of the spread can be described by the linear dependency, and the fitted constant B is 0.81. Finally, the simulated evolution of the droplet height is in good agreement with the exponential decay dependency during all the spread and equilibrium stages. The fitted constant C_2 equals to 1.25, which is similar to the experimentally fitted constant 1.42 in Ref. [9].

As a summary of the above results, we find that both liquid surface tension and viscosity can influence the droplet dynamics in the horizontal and vertical directions, especially after the equilibrium stage. Owing to the much lower Oh in the previous studies [7–11], the inertia is regarded as having the dominant effect, and the viscous effect is ignored. However, the minimum Oh = 0.02 in our studies is larger than the critical value 0.018 [20,22]. This suggests that viscosity should play a role in droplet dynamics. Additionally, the maximum capillary number (ratio between the viscous force and the capillary force) in our study is $\mathrm{Ca} = \mu \mathrm{V}/[(1-\phi)\gamma] \sim 0.1$ [44,45]. This implies that the capillary force is 10 times the viscosity force. Thus the capillary effect and viscosity effect can significantly affect droplet dynamics.

Both the velocity vector and velocity contours of the droplet at the end of the equilibrium stage ($T^* = 1.7$) are plotted in Fig. 9. By comparing droplets with different surface tensions, Fig. 9(a) shows that for the larger surface tension droplet, a significant backflow occurs at the edge of the droplet pancake. And for the lower surface tension droplet [Fig. 9(b)], its horizontal spread velocity and vertical jet velocity are higher than those of the higher surface tension droplet. This can

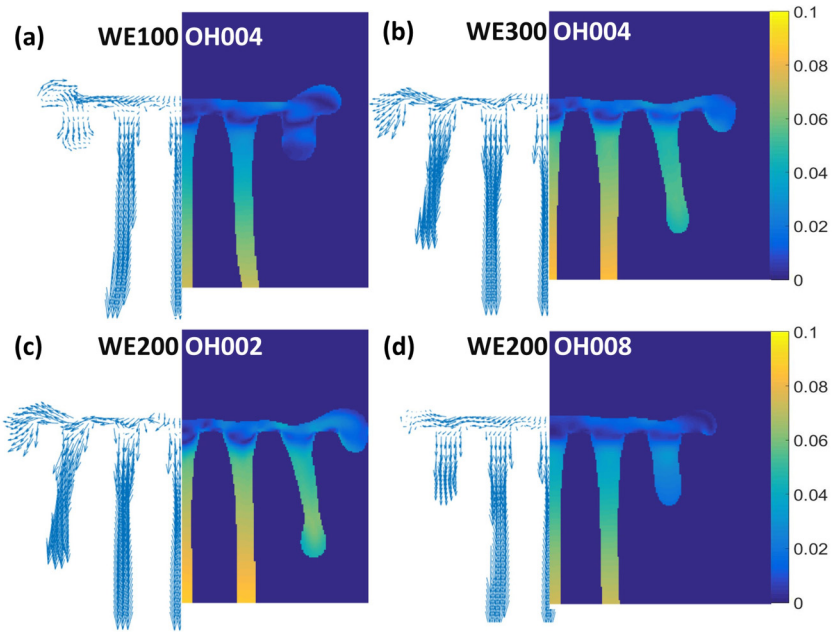

FIG. 9. The velocity vector and velocity contours of the droplet at the later equilibrium stage ($T^* = 1.7$): (a) We = 100, Oh = 0.04; (b) We = 300, Oh = 0.04; (c) We = 200, Oh = 0.02; and (d) We = 200, Oh = 0.08.

explain why the maximum spreading diameter of the larger surface tension droplet is smaller and its retraction time is shorter. Also, the higher jet velocity implies larger penetration energy, which is the reason for the larger surface tension droplet to show rebound (see the solid square in Fig. 8) while the lower surface tension droplet penetrates through the mesh array at the retraction stage (see the solid inverted triangle in Fig. 8). On the other hand, by comparing droplets with different viscosities, it can be observed that for the larger viscosity droplet [Fig. 9(d)], its horizontal spread velocity and vertical jet velocity are significantly lower than those of the smaller viscosity droplet owing to the viscous energy dissipation, which finally results in a lower maximum spread diameter.

To further quantitatively investigate the influence of the droplet properties on the droplet dynamics, the maximum spreading diameter of the pancake and the maximum liquid jet breakup length have been recorded. Figure 10(a) represents how the maximum pancake spreading diameters are affected when impacting the mesh array with different Weber and Ohnesorge numbers. In agreement with the droplet evolution process shown in Fig. 7, the maximum pancake spreading diameter increases with We and decreases with the increase of Oh. Kumar *et al.* [7] and Zhang *et al.* [8] proposed that the maximum droplet spreading diameter scales as $\sim \mathrm{We}^{0.25}$ based on an analysis of the balance between droplet's dynamic pressure and capillary pressure in the configuration of droplet impacting on a flat hydrophobic plate.

In this study the prediction is extended to higher viscosity droplet cases. Following the theory proposed by Scheller *et al.* [46], by balancing the droplet dynamic energy, surface energy, and viscous dissipation energy, the maximum spreading diameter of a droplet impacting on the flat plate scales as $\sim (\mathrm{We}/\mathrm{Oh})^{0.166}$ [36,46]. Considering the droplet viscous dissipation is larger when forced crossing the perforated plate [16,17] than impacting a flat plate, a modified model is obtained by adding a correction term containing Oh:

$$D^*_{\max} = 0.61 * \left(\frac{\mathrm{We}}{\mathrm{Oh} + 0.063} \right)^{0.166}. \tag{3}$$

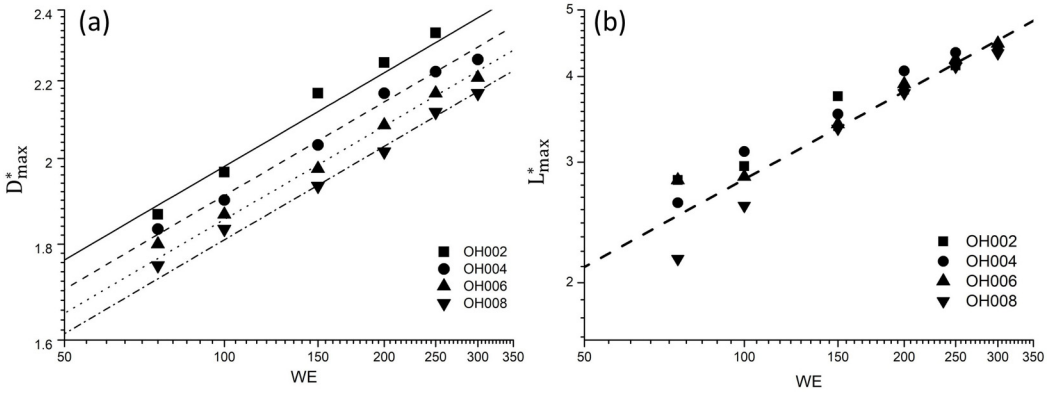

FIG. 10. The effects of Weber and Ohnesorge numbers on the maximum dimensionless pancake spreading diameter and maximum jet breakup length.

D^*_{max} is the maximum dimensionless spreading diameter of the pancake. As shown in Fig. 10(a), the predictions of the modified model agree with the simulation results over a wide range of We at Oh = 0.02, 0.04, 0.06, and 0.08, respectively.

Figure 10(b) presents the maximum liquid jet breakup length versus different Weber and Ohnesorge numbers. As shown in the graph, compared with Oh, We has a dominant effect on the liquid jet breakup length. According to Grant *et al.* [38], for the weakly turbulent liquid column, the ratio of maximum jet breakup length (L_{max}) and opening width (w) can be scaled as

$$\frac{L_{max}}{w} \sim \left[\sqrt{\mathrm{We}^*}(1+3\cdot \mathrm{Oh}^*)\right]^{0.85}, \tag{4}$$

where We* and Oh* are the modified Weber and Ohnesorge numbers which integrate the influence of drop speed and mesh size. According to Wang *et al.* [21], the droplet penetration velocity (V_P) when impacting the mesh can be expressed as $V_P^2 \sim \sqrt{2}\pi w V^2/\mathrm{D}_0$. Based on the balance of the droplet inertial force $\sim 0.5\rho_l V_P^2$, capillary force $\sim 4\gamma/w$, and viscous drag $\sim \mu V_P/w$, We* and Oh* can be written as $\mathrm{We}^* = (\sqrt{2}\pi w^2/8D_0^2)\mathrm{We}$ and $\mathrm{Oh}^* = (\mathrm{D}_0/2w)^{0.5}\mathrm{Oh}$, respectively. Due to the small magnitude of the modified Oh $\mathrm{Oh}^* \sim 10^{-2}$, the viscosity term in Eq. (4) can be neglected. Substituting We* into Eq. (4), the maximum dimensionless breakup length (L^*_{max}) can be described as

$$L^*_{max} = \frac{L_{max}}{D_0} \sim \left(\frac{w}{D_0}\right)\left(\frac{\sqrt{2}\pi w^2}{8D_0^2}\mathrm{We}\right)^{0.425}. \tag{5}$$

The best fitted Eq. (5) $L^*_{max} = 0.4(\mathrm{We})^{0.425}$ is plotted as the dashed line in Fig. 10(b), where the constant 0.4 is of the same magnitude as the experimentally fitted constant in Ref. [38]. As shown in the graph, deviations from the model occur mainly under the lower Weber numbers for larger Oh cases, where the capillary effect dominates the droplet dynamics and the viscosity effect of the ambient gas cannot be ignored [37]. However, with the larger Weber numbers, in which the inertial effect governs the droplet dynamics, the modified equation achieves a good agreement with the simulation results.

B. Droplet energy evolution

The energy analysis is adopted to further investigate the droplet fragmentation mechanism. The droplet kinetic energy (KE) is represented by $\iiint \frac{1}{2}\rho_l V^2 d\Omega$, and surface energy (SE) is calculated by γS, where Ω is the droplet volume and S is the liquid interface area. The viscous energy dissipation

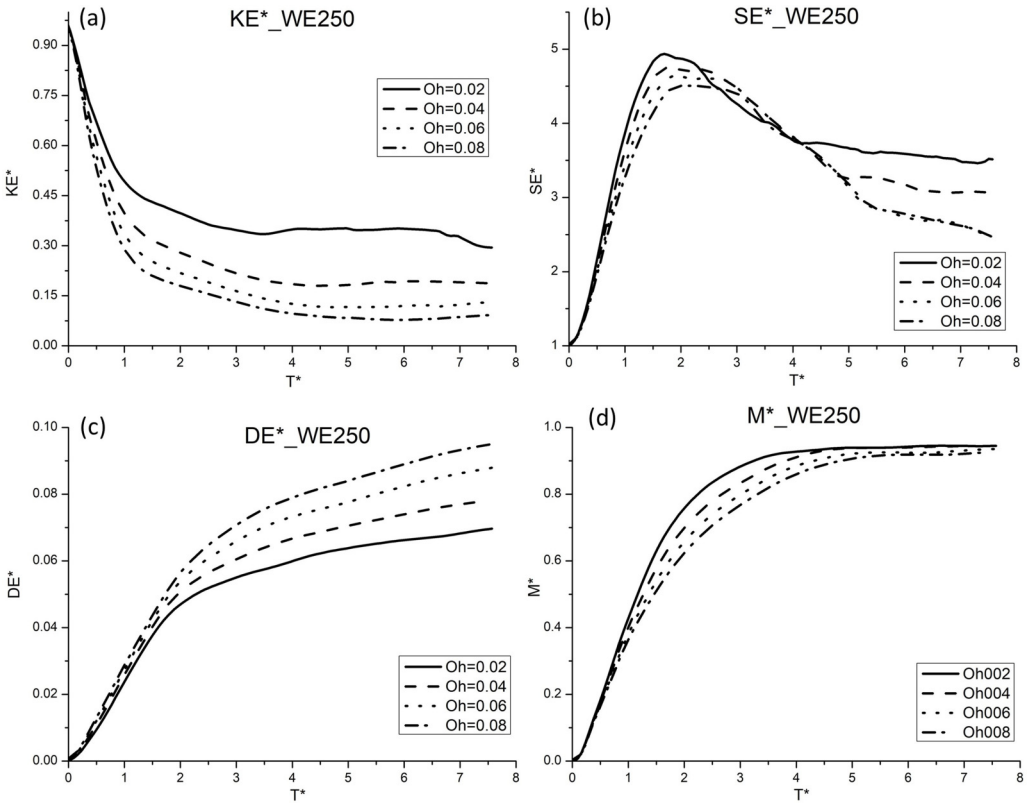

FIG. 11. The dimensionless kinetic energy (a), surface energy (b), viscous energy dissipation (c), and penetrated mass (d) evolution for the We = 250 cases.

(DE) is described as

$$\mathrm{DE} = \int_0^N \int_0^\Omega \Theta d\Omega dt, \tag{6}$$

$\int_0^\Omega \Theta d\Omega$ represents the droplet viscous dissipation rate (VDR), and [47]

$$\Theta = \mu\left[2\left(\frac{\partial u}{\partial x}\right)^2 + 2\left(\frac{\partial v}{\partial y}\right)^2 + 2\left(\frac{\partial w}{\partial z}\right)^2 + \left(\frac{\partial u}{\partial y} + \frac{\partial v}{\partial x}\right)^2 + \left(\frac{\partial v}{\partial z} + \frac{\partial w}{\partial y}\right)^2 + \left(\frac{\partial w}{\partial x} + \frac{\partial u}{\partial z}\right)^2\right], \tag{7}$$

where u, v, w stand for the velocity components in x, y, z directions, respectively. The following Figs. 11 and 12 present the droplet energy and penetrated mass evolution for We = 200 and Oh = 0.04 cases before $T^* = 8$, respectively. The dimensionless energy KE*, SE* are normalized by their initial values, respectively. DE* equals DE divided by the droplet total energy, which equals the sum of the initial SE and KE. The dimensionless penetrated mass M^* is calculated by the penetrated mass below the mesh array divided by the droplet initial mass.

As demonstrated in Figs. 11 and 12, upon the droplet contacting with the plate, KE is partly converted into SE and partly dissipated through DE. With the droplet spreading and the liquid jets below the plate continuously developing, SE reaches its peak value very quickly. In the meantime, owing to the interaction between the droplet and the solid array during the spread and permeation processes, DE significantly increases. Then, due to the capillary instability, the liquid jets break up, which leads to a lower level of SE [39,48]. The droplet-penetrated mass first increases and then

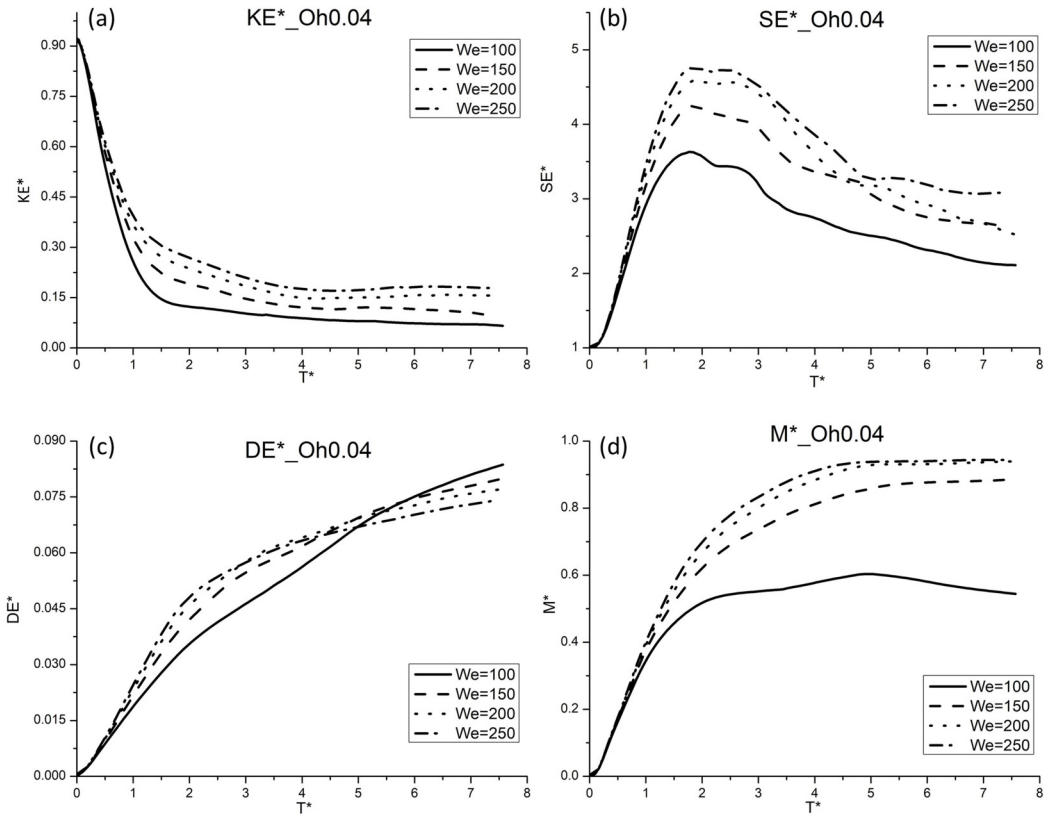

FIG. 12. The dimensionless kinetic energy (a), surface energy (b), viscous energy dissipation (c), and penetrated mass (d) evolution for the Oh = 0.04 cases.

reaches a quasiequilibrium. The evolution of the droplet energy and penetrated mass is consistent with its dynamic process shown in Fig. 5.

For the same We, Fig. 11(a) indicates that the lower Oh droplet achieves a higher final KE, which can be explained by the lower viscosity dissipation [see Fig. 11(c)]. It also can be observed that the lower Oh cases reach higher maximum surface energy [see Fig. 11(b)], which agrees with the prediction [Eq. (3)] of the maximum pancake spreading diameter. As indicated in Fig. 11(d), owing to the high We (We = 250) in the presented case, the penetration of the droplet is dominated by the inertial effect, and thus the liquid viscosity has little influence on its total penetrated mass. It is also noted that the viscous drag is lower for the lower Oh cases, which eventually results in a faster penetration rate.

For the same Oh, larger surface tension causes more obstruction to the spread of the droplet over the plate and to the penetration of liquid through the mesh openings. Thus the final KE and SE are lower for the smaller We cases [shown in Figs. 12(a) and 12(b)]. Also, owing to the larger maximum surface area for the higher We droplet, its viscosity dissipation is higher before the droplet fragmentation [shown in Fig. 12(c)]. Figure 12(d) indicates that the surface tension of the droplet significantly influences its total penetrated mass. During the droplet penetration, the capillary force for a single jet scales as $4\gamma/w$; thus a higher surface tension droplet implies a higher capillary force. As shown in Fig. 14(a), under the same dimensionless time, the droplet jet length is longer for the higher We cases, which results in a larger total penetrated mass.

As shown in Figs. 11(b) and 12(b), the droplet surface energy significantly decreases after liquid jet breakup. The value of the droplet surface area can be obtained through dividing the droplet SE by

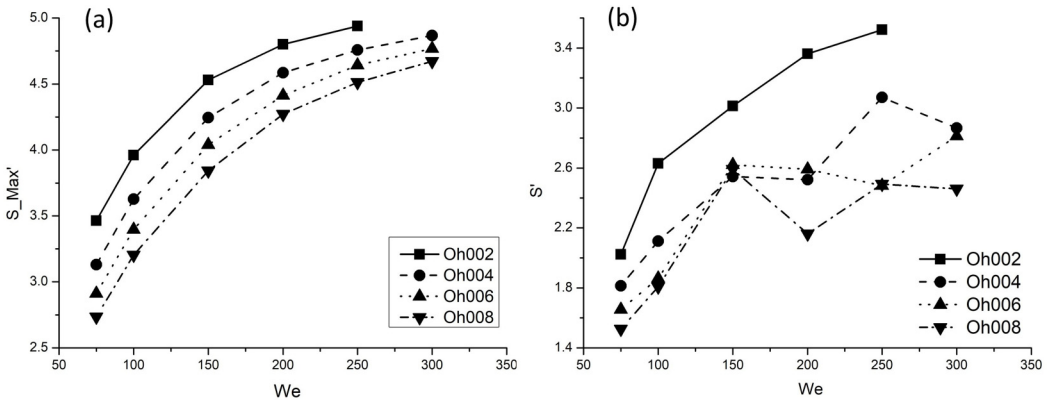

FIG. 13. The maximum dimensionless droplet spreading surface area (a) and the total liquid surface area after jet breakup (b) vs We, for various Oh cases.

its surface tension. Figure 13 shows the maximum droplet spreading surface area and the total liquid surface area after jet breakup, as the two surface areas are the critical parameters in the application of materials science and spray cooling [7,8]. The x axis represents We, and the y axis in Figs. 13(a) and 13(b) stands for the dimensionless form of the maximum droplet spreading surface area and the total liquid surface area after fragmentation (when $T^* = 7.5$), respectively.

In agreement with the SE evolution results in Figs. 11 and 12, the maximum droplet spreading surface area increases with We but decreases with Oh. This is because higher surface tension and viscosity drag tend to prevent the droplet from spreading. However, as shown in Fig. 13(b), the total liquid surface area after jet breakup is affected by different mechanisms for different Ohnesorge numbers. For an Oh closes to the critical value of 0.018, the total liquid surface area after fragmentation is larger than the other cases and increases with We. However, when Oh is greater than the critical value, the total liquid surface area varies in different cases and is significantly below the maximum value. The differences can be explained via the mechanism of the jet breakup.

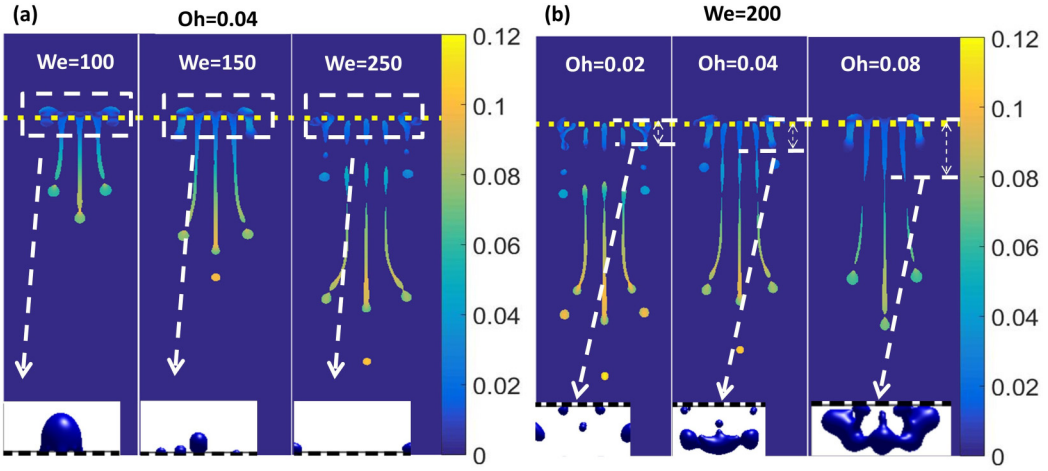

FIG. 14. The droplet velocity contour in the symmetry plane: (a) Oh = 0.04 droplets, with We = 100, 150, and 250, respectively; (b) We = 200 droplets, with Oh = 0.02, 0.04, and 0.08, respectively. The 3D inserted figures in (a) represent the droplet remaining above the plate and in (b) show the merged droplets after the jet fragmentation.

The unstable wavelength for jet breakup increases with liquid viscosity, which results in a bigger satellite droplet diameter for a higher Oh [49–51]. When the satellite droplet diameter is smaller than the width of the solid bridge between neighboring mesh openings, drops drip down dispersedly [Oh = 0.02, shown in Fig. 14(b)]. Thus a higher We leads to a longer liquid jet [shown in Fig. 14(a)], finally resulting in a higher total liquid surface area after fragmentation. For a satellite droplet diameter larger than the solid bridge breadth, the satellite droplets near the bottom of the plate merge together, which leads to decreased total liquid surface area [the Oh = 0.04 and 0.08 cases in Fig. 14(b)].

IV. CONCLUSION

In this study we adopt a nonorthogonal multiple-relaxation-time lattice Boltzmann method to simulate a droplet impacting on a mesh array. The methodology has been validated using experimental data of a droplet impact on a solid surface. The validated method has been employed to simulate a droplet impacting on a mesh array over a wide range of liquid properties, with a focus on the influences of the liquid surface tension and viscosity. The results indicate that during the initial impact and spread stage of the droplet impact, its dynamics is dominated by the inertial effect, and the liquid properties have little influence. The droplet spreads on the mesh plate to form a pancake whose diameter and height can be predicted by models of a power law [Eq. (1)] and an exponential decay dependency [Eq. (2)], respectively. As the droplet continuously spreads, liquid starts to penetrate through mesh openings and forms jets below the mesh plate. The liquid viscous drag and surface tension act to prevent the horizontal spread of the droplet and the vertical penetration. The maximum pancake spreading diameter is a function of Weber and Ohnesorge numbers, as described by Eq. (3). The liquid jets below the mesh plate are affected by a combination of the inertia force and capillary force, with the capillary effect being dominant. The liquid jets eventually break up due to jet instability, and the maximum breakup length can be predicted by Eq. (5).

More quantitative analyses are carried out from the perspective of energy evolution, penetrated mass, and surface area to further explore the effects of liquid properties. Based on the droplet energy evolution, the higher surface tension and viscosity result in lower kinetic energy and higher viscous energy dissipation due to the obstruction of the droplet movement. In terms of the penetrated mass, the results suggest that the viscous effect reduces the droplet penetration rate but has little influence on the total penetrated mass. The total penetrated mass significantly decreases with the increasing surface tension, which can be explained by the capillary effect on the liquid jet. Moreover, based on the analysis of the droplet surface area, the maximum droplet spreading surface area decreases with the increasing surface tension and viscosity. Finally, the total liquid surface area after jet breakup is significantly influenced by the liquid viscosity. A lower viscosity leads to a shorter unstable wavelength of the liquid jet and thus smaller dispersed satellite droplets, while a higher viscosity results in a longer unstable wavelength and thus bigger merged satellite droplets. These findings are expected to be valid for even a wider range of Weber and Ohnesorge numbers, which should be confirmed in follow-up studies. Also, in the future it would be informative to consider the effects of mesh array vibration due to droplet impact on the mesh array.

ACKNOWLEDGMENTS

This work was supported by the UK Engineering and Physical Sciences Research Council (EPSRC) under the project UK Consortium on Mesoscale Engineering Sciences (UKCOMES) (Grant No. EP/R029598/1) and the project “HiLeMMS”: High-Level Mesoscale Modelling System (Grant No. EP/P022243/1).

APPENDIX

The nonorthogonal multiple-relaxation-time lattice Boltzmann model can be described as [31]:

$$f_i^*(\boldsymbol{x},t) = f_i(\boldsymbol{x},t) - \boldsymbol{\Lambda}\left[f_i - f_i^{eq}\right]_{(x,t)} + \frac{\Delta t}{2}[\bar{F}_i(\boldsymbol{x},t) + \bar{F}_i(\boldsymbol{x}+\boldsymbol{e_i}\Delta t, t+\Delta t)], \tag{A1}$$

where f_i and f_i^* are discrete distribution functions before and after collision, respectively, $\boldsymbol{x}$ represents the position vector, t is the time, $\bar{F}_i$ stands for the forcing terms in the discrete velocity space, and $\boldsymbol{e}_i$ are the discrete velocities. The collision operator is $\boldsymbol{\Lambda} = (\boldsymbol{M}^{-1}\boldsymbol{S}\boldsymbol{M})$, where $\boldsymbol{M}$ is the transformation matrix which depends on the raw moment set, and $\boldsymbol{S}$ is a diagonal relaxation matrix [23,17].

The low-Mach equilibrium distribution function f_i^{eq} is given as [52]

$$f_i^{eq} = \rho\omega(|\boldsymbol{e}_i|^2)\left[1 + \frac{\boldsymbol{e}_i\cdot\boldsymbol{u}}{c_s^2} + \frac{(\boldsymbol{e}_i\cdot\boldsymbol{u})^2}{2c_s^4} - \frac{(\boldsymbol{u}\cdot\boldsymbol{u})}{2c_s^2}\right], \tag{A2}$$

where ρ stands for density, c_s is the lattice sound speed and equals $1/\sqrt{3}$, and $\boldsymbol{u} = [u_x, u_y, u_z]$ represents the fluid velocity tensor. In this work, the D3Q19 lattice model is used. The weights for the D3Q19 lattice model are $\omega(0) = 1/3$, $\omega(1) = 1/18$, and $\omega(2) = 1/36$. The discrete velocities $\boldsymbol{e}_i = [|e_{ix}\rangle, |e_{iy}\rangle, |e_{iz}\rangle,]$ are defined as follows:

$$\begin{aligned}
|e_{ix}\rangle &= [0,\ 1,-1,\ 0,\ 0,\ 0,\ 0,\ 1,-1,\ 1,-1,\ 1,-1,\ 1,-1,\ 0,\ 0,\ 0,\ 0,\ 1,\\
&\quad -1,\ 1,-1,\ 1,-1,\ 1,-1]^{\mathrm{T}},\\
|e_{iy}\rangle &= [0,\ 0,\ 0,\ 1,-1,\ 0,\ 0,\ 1,\ 1,-1,-1,\ 0,\ 0,\ 0,\ 0,\ 1,-1,\ 1,\\
&\quad -1,\ 1,\ 1,-1,-1,\ 1,\ 1,-1,-1]^{\mathrm{T}},\\
|e_{iz}\rangle &= [0,\ 0,\ 0,\ 0,\ 0,\ 1,-1,\ 0,\ 0,\ 0,\ 0,\ 1,\ 1,-1,\\
&\quad -1,\ 1,\ 1,-1,-1,\ 1,\ 1,\ 1,\ 1,-1,-1,-1,-1]^{\mathrm{T}},
\end{aligned}$$

where $i = 0, 1, \ldots, 18$, $|\cdot\rangle$ denotes a 19-dimensional column vector, and the superscript T denotes the transposition. The forcing terms can be written as [52]

$$\bar{F}_i = \omega(|\boldsymbol{e}_i|^2)\left[\frac{\boldsymbol{e}_i - \boldsymbol{u}}{c_s^2} + \frac{(\boldsymbol{e}_i\cdot\boldsymbol{u})\boldsymbol{e}_i}{c_s^4}\right]\cdot\boldsymbol{F}, \tag{A3}$$

where $\boldsymbol{F} = [F_x, F_y, F_z]$ is the total force vector imposed on the fluid. Multiplication of the explicit form of Eq. (A1) by the transformation matrix $\boldsymbol{M}$ leads to the collision equation in the moment space as follows [23]:

$$\bar{\boldsymbol{m}}^* = \bar{\boldsymbol{m}} - \boldsymbol{S}(\bar{\boldsymbol{m}} - \boldsymbol{m}^{\boldsymbol{eq}}) + \left(\boldsymbol{I} - \frac{\boldsymbol{S}}{2}\right)\Delta t\tilde{\boldsymbol{F}}, \tag{A4}$$

where $\boldsymbol{I}$ is the unit matrix, and the transformation $\overline{f_i} = f_i - \Delta t\bar{F}_i/2$ has been used to remove the implicit scheme in Eq. (A1), $\bar{\boldsymbol{m}} = \boldsymbol{M}\bar{\boldsymbol{f}}$, $\boldsymbol{m}^{\boldsymbol{eq}} = \boldsymbol{M}\boldsymbol{f}^{\boldsymbol{eq}}$, and $\tilde{\boldsymbol{F}} = \boldsymbol{M}\bar{\boldsymbol{F}}$. Following the collision step, the discrete distribution functions are obtained by $\bar{f}_i^* = \boldsymbol{M}^{-1}\bar{\boldsymbol{m}}^*$. By moving from position $\boldsymbol{x}$ to the neighboring positions $(\boldsymbol{x} + \boldsymbol{e}_i\Delta t)$ along the discrete velocity directions, the updated discrete distribution functions are

$$\bar{f}_i(\boldsymbol{x} + \boldsymbol{e}_i\Delta t, t + \Delta t) = \bar{f}_i^*(\boldsymbol{x}, t). \tag{A5}$$

The fluid properties in the physical space can be calculated by

$$\rho = \sum_i \bar{f}_i, \quad \rho\boldsymbol{u} = \sum_i \bar{f}_i\boldsymbol{e}_i + \frac{\Delta t\boldsymbol{F}}{2}. \tag{A6}$$

In this paper the corresponding nonorthogonal transformation matrix $\boldsymbol{M}$ following the latest advances in cascaded lattice Boltzmann scheme [53,54] is employed. It can be proven through a Chapman-Enskog analysis (see Appendix A in Ref. [23]) that such a nonorthogonal MRT-LBM recovers the Navier-Stokes equations in the low-Mach-number limit.

To simulate the multiphase flow, the pseudopotential model is adopted in which the molecular interactions that lead to the phase segregation between phases are represented by a pseudopotential interaction force [28]:

$$\boldsymbol{F}_{\mathbf{int}} = -G\psi(\boldsymbol{x})\sum_i w(|\boldsymbol{e}_i|^2)\psi(\boldsymbol{x}+\boldsymbol{e}_i\Delta t)\boldsymbol{e}_i, \tag{A7}$$

where G is the interaction strength which is usually fixed as -1, ψ is the pseudopotential which is dependent on density, and the weights are $w(|\boldsymbol{e}_i|^2) = \omega(|\boldsymbol{e}_i|^2)/c_s^2$. Following Colosqui *et al.* and Yuan and Schaefer [55,56], the pseudopotential is expressed as

$$\psi = \sqrt{\frac{2\left(p_{\mathrm{EOS}} - \rho c_s^2\right)}{Gc^2}}, \tag{A8}$$

where $c = 1$ is the lattice constant, and p_{EOS} is related to the equation of state (EOS). In this work the piecewise equation of state is adopted [56]. In addition, the following terms are added to $\bar{\boldsymbol{F}}_{\boldsymbol{i}}$ to describe the interaction between the fluid and a solid surface [31]:

$$\boldsymbol{F}_{\mathbf{ads}} = -G_{\mathrm{ads}}\psi(\boldsymbol{x})\sum_i w(|\boldsymbol{e}_i|^2)\psi(\boldsymbol{x})s(\boldsymbol{x}+\boldsymbol{e}_i\Delta t)\boldsymbol{e}_i, \tag{A9}$$

where G_{ads} is the fluid-solid interaction strength to adjust the droplet contact angle, and $s(\boldsymbol{x})$ is an indicator function which equals 1 for solid and 0 for fluid, respectively. To achieve a large density ratio and tunable surface tension for multiphase flow in such a nonorthogonal MRT-LBM, several elements in $\tilde{\boldsymbol{F}}$ should be modified. The detailed derivations and explanations for such a modification can be seen in the study of Fei *et al.* [23].

[1] J. P. Rothstein, Slip on superhydrophobic surfaces, Annu. Rev. Fluid Mech. **42**, 89 (2010).

[2] G. S. Watson, M. Gellender, and J. A. Watson, Self-propulsion of dew drops on lotus leaves: A potential mechanism for self-cleaning, Biofouling **30**, 427 (2014).

[3] F. Liu, G. Ghigliotti, J. J. Feng, and C. H. Chen, Numerical simulations of self-propelled jumping upon drop coalescence on non-wetting surfaces, J. Fluid Mech. **752**, 39 (2014).

[4] E. P. Ivanova, J. Hasan, H. K. Webb, V. K. Truong, G. S. Watson, J. A. Watson, and C. Löbbe, Natural bactericidal surfaces: Mechanical rupture of *Pseudomonas aeruginosa* cells by cicada wings, Small **8**, 2489 (2012).

[5] K. Ostrikov, M. Macgregor-Ramiasa, A. Cavallaro, K. K. Ostrikov, and K. Vasilev, Bactericidal effects of plasma-modified surface chemistry of silicon nanograss, J. Phys. D: Appl. Phys. **49**, 304001 (2016).

[6] C. H. Choi and C. J. Kim, Large Slip of Aqueous Liquid Flow over a Nanoengineered Superhydrophobic Surface, Phys. Rev. Lett. **96**, 066001 (2006).

[7] A. Kumar, A. Tripathy, Y. Nam, C. Lee, and P. Sen, Effect of geometrical parameters on rebound of impacting droplets on leaky superhydrophobic meshes, Soft Matter **14**, 1571 (2018).

[8] G. Zhang, M. A. Quetzeri-Santiago, C. A. Stone, L. Botto, and J. R. Castrejón-Pita, Droplet impact dynamics on textiles, Soft Matter **14**, 8182 (2018).

[9] S. A. Kooij, A. M. Moqaddam, T. C. de Goede, D. Derome, J. Carmeliet, N. Shahidzadeh, and D. Bonn, Sprays from droplets impacting a mesh, J. Fluid Mech. **871**, 489 (2019).

[10] P. Brunet, F. Lapierre, F. Zoueshtiagh, V. Thomy, and A. Merlen, To grate a liquid into tiny droplets by its impact on a hydrophobic microgrid, Appl. Phys. Lett. **95**, 254102 (2009).

[11] D. Soto, H. L. Girard, A. Le Helloco, T. Binder, D. Quéré, and K. K. Varanasi, Droplet fragmentation using a mesh, Phys. Rev. Fluids **3**, 083602 (2018).
[12] J. Ebert, E. Özkol, A. Zeichner, K. Uibel, Ö. Weiss, U. Koops, and H. Fischer, Direct inkjet printing of dental prostheses made of zirconia, J. Dent. Res. **88**, 673 (2009).
[13] R. Jonczyk, T. Kurth, A. Lavrentieva, J. G. Walter, T. Scheper, and F. Stahl, Living cell microarrays: An overview of concepts, Microarrays **5**, 11 (2016).
[14] B. Derby, Inkjet printing ceramics: From drops to solid, J. Eur. Ceram. Soc. **31**, 2543 (2011).
[15] C. D. Modak, A. Kumar, A. Tripathy, and P. Sen, Drop impact printing, Nat. Commun. **11**, 4327 (2020).
[16] U. Sen, T. Roy, S. Chatterjee, R. Ganguly, and C. M. Megaridis, Post-impact behavior of a droplet impacting on a permeable metal mesh with a sharp wettability step, Langmuir **35**, 12711 (2019).
[17] G. Wang, L. Fei, and K. H. Luo, Lattice Boltzmann simulation of water droplet impacting a hydrophobic plate with a cylindrical pore, Phys. Rev. Fluids **5**, 083602 (2020).
[18] S. Ryu, P. Sen, Y. Nam, and C. Lee, Water Penetration through a Superhydrophobic Mesh During a Drop Impact, Phys. Rev. Lett. **118**, 014501 (2017).
[19] J. Xu, J. Xie, X. He, Y. Cheng, and Q. Liu, Water drop impacts on a single-layer of mesh screen membrane: Effect of water hammer pressure and advancing contact angles, Exp. Therm. Fluid Sci. **82**, 83 (2017).
[20] K. Vontas, C. Boscariol, M. Andredaki, A. Georgoulas, C. Crua, J. H. Walther, and M. Marengo, Droplet impact on suspended metallic meshes: Effects of wettability, Reynolds and Weber numbers, Fluids **5**, 81 (2020).
[21] L. Wang, X. Wu, W. Yu, P. Hao, F. He, and X. Zhang, Numerical study of droplet fragmentation during impact on mesh screens, Microfluid. Nanofluid. **23**, 136 (2019).
[22] F. Blanchette and T. P. Bigioni, Partial coalescence of drops at liquid interfaces, Nat. Phys. **2**, 254 (2006).
[23] L. Fei, J. Du, K. H. Luo, S. Succi, M. Lauricella, A. Montessori, and Q. Wang, Modeling realistic multiphase flows using a non-orthogonal multiple-relaxation-time lattice Boltzmann method, Phys. Fluids **31**, 042105 (2019).
[24] Q. Li, K. H. Luo, Q. J. Kang, Y. L. He, Q. Chen, and Q. Liu, Lattice Boltzmann methods for multiphase flow and phase-change heat transfer, Prog. Energy Combust. Sci. **52**, 62 (2016).
[25] L. Fei, J. Yang, Y. Chen, H. Mo, and K. H. Luo, Mesoscopic simulation of three-dimensional pool boiling based on a phase-change cascaded lattice Boltzmann method, Phys. Fluids **32**, 103312 (2020).
[26] L. Fei, K. H. Luo, C. Lin, and Q. Li, Modeling incompressible thermal flows using a central-moments-based lattice Boltzmann method, Int. J. Heat Mass Transfer **120**, 624 (2018).
[27] L. Chen, Q. Kang, Y. Mu, Y. L. He, and W. Q. Tao, A critical review of the pseudopotential multiphase lattice Boltzmann model: Methods and applications, Int. J. Heat Mass Transfer **76**, 210 (2014).
[28] X. Shan and H. Chen, Lattice Boltzmann model for simulating flows with multiple phases and components, Phys. Rev. E **47**, 1815 (1993).
[29] S. Chen and G. D. Doolen, Lattice Boltzmann method for fluid flows, Annu. Rev. Fluid Mech. **30**, 329 (1998).
[30] H. Huang, D. T. Thorne Jr., M. G. Schaap, and M. C. Sukop, Proposed approximation for contact angles in Shan-and-Chen-type multicomponent multiphase lattice Boltzmann models, Phys. Rev. E **76**, 066701 (2007).
[31] Q. Li, K. H. Luo, and X. J. Li, Lattice Boltzmann modeling of multiphase flows at large density ratio with an improved pseudopotential model, Phys. Rev. E **87**, 053301 (2013).
[32] Q. Li, K. H. Luo, Q. J. Kang, and Q. Chen, Contact angles in the pseudopotential lattice Boltzmann modeling of wetting, Phys. Rev. E **90**, 053301 (2014).
[33] S. Mukherjee, A. Zarghami, C. Haringa, K. van As, S. Kenjereš, and H. E. Van den Akker, Simulating liquid droplets: A quantitative assessment of lattice Boltzmann and volume of fluid methods, Int. J. Heat Fluid Flow **70**, 59 (2018).
[34] B. E. Rapp, *Microfluidics: Modeling, Mechanics and Mathematics* (William Andrew Publishing, Norwich, NY, 2016).
[35] A. Bedarkar, X. F. Wu, and A. Vaynberg, Wetting of liquid droplets on two parallel filaments, Appl. Surf. Sci. **256**, 7260 (2010).

[36] A. L. Yarin, Drop impact dynamics: Splashing, spreading, receding, bouncing …, Annu. Rev. Fluid Mech. **38**, 159 (2006).
[37] K. A. Sallam, Z. Dai, and G. M. Faeth, Liquid breakup at the surface of turbulent round liquid jets in still gases, Int. J. Multiphase Flow **28**, 427 (2002).
[38] R. P. Grant and S. Middleman, Newtonian jet stability, AIChE J. **12**, 669 (1966).
[39] S. P. Lin and R. D. Reitz, Drop and spray formation from a liquid jet, Annu. Rev. Fluid Mech. **30**, 85 (1998).
[40] D. Richard, C. Clanet, and D. Quéré, Contact time of a bouncing drop, Nature (London) **417**, 811 (2002).
[41] R. Rioboo, M. Marengo, and C. Tropea, Time evolution of liquid drop impact onto solid, dry surfaces, Exp. Fluids **33**, 112 (2002).
[42] G. Lagubeau, M. A. Fontelos, C. Josserand, A. Maurel, V. Pagneux, and P. Petitjeans, Spreading dynamics of drop impacts, J. Fluid Mech. **713**, 50 (2012).
[43] C. Josserand and S. T. Thoroddsen, Drop impact on a solid surface, Annu. Rev. Fluid Mech. **48**, 365 (2016).
[44] A. Delbos, E. Lorenceau, and O. Pitois, Forced impregnation of a capillary tube with drop impact, J. Colloid Interface Sci. **341**, 171 (2010).
[45] D. Or, Scaling of capillary, gravity and viscous forces affecting flow morphology in unsaturated porous media, Adv. Water Res. **31**, 1129 (2008).
[46] B. L. Scheller and D. W. Bousfield, Newtonian drop impact with a solid surface, AIChE J. **41**, 1357 (1995).
[47] C. He, X. Xia, and P. Zhang, Non-monotonic viscous dissipation of bouncing droplets undergoing off-center collision, Phys. Fluids **31**, 052004 (2019).
[48] M. Goldin, J. Yerushalmi, R. Pfeffer, and R. Shinnar, Breakup of a laminar capillary jet of a viscoelastic fluid, J. Fluid Mech. **38**, 689 (1969).
[49] L. Rayleigh, On the instability of jets, Proc. London Math. Soc. **10**, 4 (1878).
[50] L. Crane, S. Birch, and P. D. McCormack, The effect of mechanical vibration on the breakup of a cylindrical water jet in air, Br. J. Appl. Phys. **15**, 743 (1964).
[51] R. J. Donnelly and W. Glaberson, Experiments on the capillary instability of a liquid jet, Proc. R. Soc. London, Ser. A **290**, 547 (1966).
[52] Z. Guo, C. Zheng, and B. Shi, Discrete lattice effects on the forcing term in the lattice Boltzmann method, Phys. Rev. E **65**, 046308 (2002).
[53] L. Fei and K. H. Luo, Consistent forcing scheme in the cascaded lattice Boltzmann method, Phys. Rev. E **96**, 053307 (2017).
[54] L. Fei, K. H. Luo, and Q. Li, Three-dimensional cascaded lattice Boltzmann method: Improved implementation and consistent forcing scheme, Phys. Rev. E **97**, 053309 (2018).
[55] C. E. Colosqui, G. Falcucci, S. Ubertini, and S. Succi, Mesoscopic simulation of non-ideal fluids with self-tuning of the equation of state, Soft Matter **8**, 3798 (2012).
[56] P. Yuan and L. Schaefer, Equations of state in a lattice Boltzmann model, Phys. Fluids **18**, 042101 (2006).